Multiple-Band Ultra-Thin Perfect Metamaterial Absorber Using Analogy Split-Ring Resonators

Ben-Xin Wang [1] · Hua-Xin Zhu [1] · Wei-Qing Huang [2]

Abstract

This paper presents a kind of perfect metamaterial absorber that can achieve multiple-band near-perfect absorption. The basic cell of the device is designed by using an analogy split-ring resonator (ASRR), an insulating dielectric sheet, and a continuous metallic board. Three discrete absorption peaks with narrow bandwidths and high absorption rates are obtained. The ratios of the dielectric sheet thickness to the wavelengths of the three absorption peaks are respectively 1/100, 1/59, and 1/43, which are all smaller than prior triple-band absorption devices. With the aid of the field distributions, the mechanism of the device is investigated. Results also demonstrate that the device performance can be controlled by the parameters (in particular of the length) of the ASRR. Based on this, a six-band terahertz metamaterial absorber is designed via simply stacking two different dimensions of ASRRs. We found that the dual-layer structure can exhibit six narrow-band absorption bands, each of which has the absorption of over 90%. The mechanism of the six-band light absorber is caused by the combination of two sets of three different modes of the two layers.

Keywords Metamaterial · Perfect absorber · Multiple-band absorption · Terahertz

Introduction

Perfect absorption devices based on metamaterials, with the ability to achieve near 100% absorption to the incident waves, have attracted widespread attention [1–15]. Various geometrical shapes of resonators, such as nano-disk [1], metallic cross [2–4], and split-ring [5–7], have been theoretically and experimentally reported to realize the perfect absorption. These devices, however, typically exhibit single-band (or single-frequency point) absorption because their unit cell has only one metallic element [1–15]. However, in many cases, such as simultaneous analysis and detection of multiple frequency points, the use of single-band absorption devices is inappropriate and unreasonable. To overcome the limitations of the single-band absorption devices, the design concept of multiple-band, in particular of triple-band absorbers is emerged [16–45]. The first presentation of the triple-band microwave absorber in the year of 2011 was made of three nested electric

closed-ring resonators [26]. Some similar structures based on three nested ring/square metallic elements were also proposed to obtain triple-band absorption [27–29]. In these structures, however, each of the resonators corresponds to an absorption peak, the superposition of the three discrete peaks results in the triple-band absorption [27–30].

There are also researchers suggesting that triple-band absorption devices can be realized by placing more (larger than 3) number of resonators in a coplanar structure. For example, four electric-field-driven resonators [31] and four spiral metallic elements [32] were designed to respectively realize the triple-band absorption. Eight electric closed-ring resonators in a coplanar structure were suggested to exhibit three distinct absorption bands at microwave region [33]. Unit cell consisting of nine elements was utilized to achieve triple-band absorption [34–40]. In these designs, each absorption peak of the triple-band devices usually corresponds to two and even three metallic elements. This is why these triple-band devices require at least four metallic elements.

To reduce the number of metallic resonators in the unit cell, simplified design of structures in achieving the triple-band absorption has been suggested [41–45]. For example, two resonators in a coplanar structure were employed to offer three microwave absorption bands [41]. Triple-band microwave absorption device was designed through using composite

✉ Ben-Xin Wang
wangbenxin@hnu.edu.cn

[1] School of Science, Jiangnan University, Wuxi 214122, China

[2] School of Physics and Electronics, Hunan University, Changsha 410082, China

structure of two metallic resonators [42]. Triple-band microwave perfect absorbers can be obtained by respectively investigating the structures of a tetra-arrow ring resonator [43] and a snowflake-shaped metallic element with spiral line [44]. Besides, a unit cell based on two modified closed-ring resonators was also presented for triple-band absorption [45].

Although these structures can achieve excellent performance of the triple-band absorption, some shortcomings are suffered from in these strategies. Firstly, the structures themselves are quite complex, and they contain many geometric parameters, which increase the optimization times and construction steps of the structure designs. Secondly, these presented triple-band absorption devices only work in the microwave region, which prohibits their practical use to some extent. Thirdly and most importantly, it is quite difficult to design perfect absorption devices with more frequency bands of such as five-band or six-band through using above- mentioned methods. Therefore, it would be nice and very useful to design a new type of perfect absorption device that can overcome these drawbacks.

In this paper, we demonstrate a kind of resonance structure that can significantly simplify the design complexity of the triple-band perfect absorption device at terahertz frequency consistimg of an Au square patch with a small rectangular notch placed on top of an insulation dielectric sheet and backed by an Au mirror. The designed structure has the ability to achieve 95.68%, 96.73%, and 95.69% absorption at frequencies of 1.77 THz, 2.99 THz, and 4.11 THz, respectively. The mechanism of the device is discussed with the aid of the field distributions in the three resonance modes. Dependence of the performance on the parametric variations of the resonator is investigated. It is revealed that the resonator length is a critical factor in controlling the resonance frequencies of the triple-band absorption device. On this basis, a six-band terahertz perfect absorption device is presented through simple stacking two similar but different dimensions of the resonators. Each layer of the structure possesses three discrete resonance peaks, the combination of the two layers leads to the six-band absorption. These characteristics of the designed devices are clearly superior to previous design of the triple-band perfect absorption devices, and therefore the devices obtained here can offer wide application prospects.

Design Principles of the Multiple-Band Perfect Metamaterial Absorber

Generally speaking, using metallic patch to achieve perfect absorption is a very simple structure design, which has been extensively demonstrated from the optical to microwave regime. Bowen et al. utilized metallic patch antenna to realize perfect absorption in a visible region [46]. Similar structure was also employed to achieve unity absorption in a microwave frequency range [47]. However, there is only one absorption peak in a specific spectrum range; this will limit their application potential in optical engineering. To increase the number of absorption peaks in this particular spectrum, the most direct and simple way is to increase the number of metallic patches in the unit cell. For example, Guo et al. employed two groups of four different sizes of metallic patches in a coplanar unit structure to achieve perfect absorption at two discrete frequencies (or dual-band perfect absorption) [36, 48]. In this frequency range, triple-band perfect absorption was obtained by adding one more group of metallic patches (i.e., three groups of nine different sizes of patches) [36]. Obviously, these devices share the same design principles that merely consider (or use) the fundamental mode resonance response of metallic patch. According to this design principle, metamaterial absorbers with four different absorption peaks at least require four groups of sixteen metallic patches having different sizes. This kind of theoretical prediction (or design principle) is verified [49, 50].

Although the use of simple design of metallic patch can have the ability to achieve perfect absorption at multiple discrete frequencies (or multiple-band perfect absorption), this kind of strategy possesses many uncontrollable issues, including complex structure design, large lattice size, time-consuming construction processes and steps, low absorption intensity, and similar or single physical mechanism. These shortcomings should be addressed when new type of multiple-band metamaterial absorbers is designed. It can be predicted that using a single metallic array to achieve multiple-band absorption can clearly overcome these mentioned issues. Therefore, the aim of this paper is to design the new type of multiple-band metamaterial absorber using as few resonators as possible (preferably one only) to address these disadvantages encountered by using many patches with different sizes.

With this idea in mind, the next challenge is how to design this metallic array structure. The first thing we think about here is the metallic patch because it is widely utilized to achieve perfect absorption at single-band, dual-band, triple-band, and even quad-band [36, 46–50]. For the patch-based absorbers, we found that the forming mechanisms of each absorption peak are all caused by the fundamental mode resonance response of the specific size of metallic patch. As a result, near-field maps of the resonance absorption peak are chiefly focused on edges of the metallic patch [36, 46–50]. It is generally known that any kind of metallic structure, including metallic patch, has only one fundamental mode resonance, which can help us understand why previous multiple-band metamaterial absorbers need many different sizes of resonators. More importantly, the near-field maps of fundamental mode resonance are symmetrically distributed at the edges of the metallic resonator (or patch) along the polarization direction (or electric field direction) of the incident

electromagnetic wave. It is important to note that the near-field maps of the fundamental mode resonance are not absolutely distributed at two edges of the metallic patch, but have a certain length of extension to the resonator from the edges of the metallic patch.

This feature gives us the opportunity to break the symmetry of the initial near-field distributions of the metallic patch by introducing some asymmetric factors, such as rectangle notch (or air gap), in the near-field enhanced areas or sections. In other words, the near-field maps of the metallic resonator could be rearranged through, for example, the introduction of the air gap in the near-field enhanced areas of the metallic patch. It can be predicted that the introduction of the air gap (or rearranged near-field distributions) in the near-field enhanced areas of the metallic patch possesses the ability to introduce some new resonance modes, and thus multiple resonance absorption peaks should be obtained. Therefore, we believe that single metamaterial resonator with slightly deformed metallic patch structure is an effective way to realize the multiple-band absorption because this kind of structure design can rearrange the near-field distributions of the resonator, introduce some new resonance modes, enrich the resonance mechanism of the multiple-band absorption, simplify structure design of the device, enhance the device absorption intensity, reduce construction process and cost, and thus the designed device is obviously different from the previous strategies using many different sizes of metallic patches and can have great application prospects in optical engineering.

Design of Triple-Band Terahertz Perfect Metamaterial Absorber

The structure schematic of the simplified design of the triple-band absorber is illustrated in Fig. 1. The device consisted of two Au layers (having the conductivity of 4.09×10^7 S/m) separated by an insulting dielectric sheet with thickness of 1.7 μm and refractive index of $n = 1.73 + i0.01$. The first Au layer is a pattern resonator formed by a square patch with a small rectangular notch. In fact, the metallic patch with an air gap has many similarities with the metallic split-ring resonator, but it is not the standard (or ordinary) metallic split-ring [51–54]; therefore, the resonator suggested here can be called the analogy split-ring resonator (ASRR). The second is a continuous film, which can block the light transmission. The square patch has the length of $l = lx = ly = 35$ μm; the small rectangular notch (or air gap) has the length of $g = 8$ μm, width of $d = 15$ μm, and deviation value of $\triangle = 8$ μm. The absorber has the period of $P = Px = Py = 42$ μm. Numerical simulations and analyses of spectral responses of the absorption device are carried out using finite-difference time domain method. A plane terahertz wave with the electric field polarized in
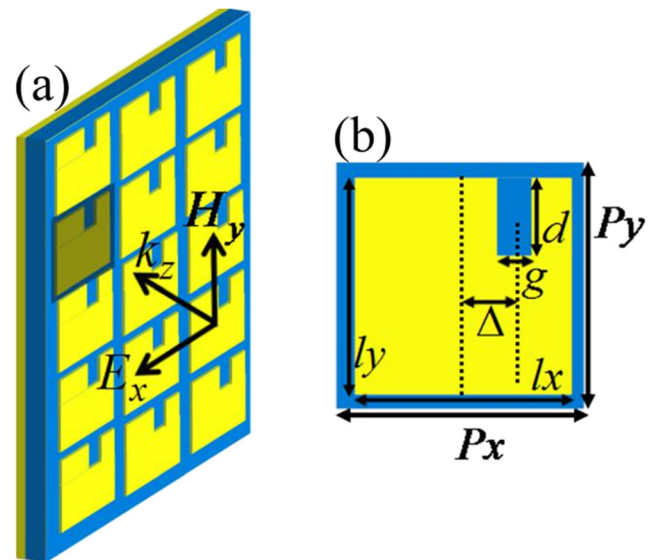

Fig. 1 **a** Structure schematic of the simplified design of the triple-band terahertz absorption device. **b** Top view of the basic cell of the designed absorber

x-axis is perpendicularly radiated into the resonance structure. Suitable boundaries of perfectly matched layers in the z direction and periodic boundary conditions in both directions of x and y are utilized.

The absorption A of the device can be expressed as $A = 1 - T - R$, where T and R are respectively the transmission and reflection of the structure. T can be totally suppressed because of the existence of the Au film, and therefore A is simplified as $A = 1 - R$. Perfect (or near-perfect) absorption can be obtained by minimizing the reflection R. Simulation results of Fig. 2a exhibit three separated resonance bands centered at 1.77 THz (M1), 2.99 THz (M2), and 4.11 THz (M3), each of peak has near 100% absorption. In addition to large absorption, the bandwidths of the three peaks (M1, M2, and M3) are quite narrow, which are respectively 0.08 THz, 0.13 THz, and 0.09 THz. The quality factors (Q, the ratio values of the frequency to the bandwidth) of modes M1, M2, and M3 are 22.13, 23.00, and 45.67, respectively. We also noted that the dielectric thickness (1.7 μm) of the device is only about 1/100, 1/59, and 1/43 of the resonance wavelengths of modes M1, M2, and M3, respectively, which indicates that the device possesses the characteristics of the deep-subwavelength scale. These excellent performances (large absorption rate, narrow absorption bandwidth, and ultra-thin dielectric thickness) are very useful in practical applications.

Compared with previous triple-band absorption devices having the shortcomings of complicated resonance structure, large size of basic cell, time-consuming construction processes and steps, low absorption intensity, and similar or single resonance mechanism [34–40, 46–50], the triple-band device presented here can not only overcome these issues but also extend the number of the resonance peaks through simply

Fig. 2 **a** Absorption spectra of the design of the triple-band terahertz absorption device. **b** Absorption spectra of the designed device in two polarization directions. **c** Absorption spectra of the designed device with the change of the period *P*. **d** Red and blue curves are respectively the simulation results of the metallic patch resonator with air gap and without
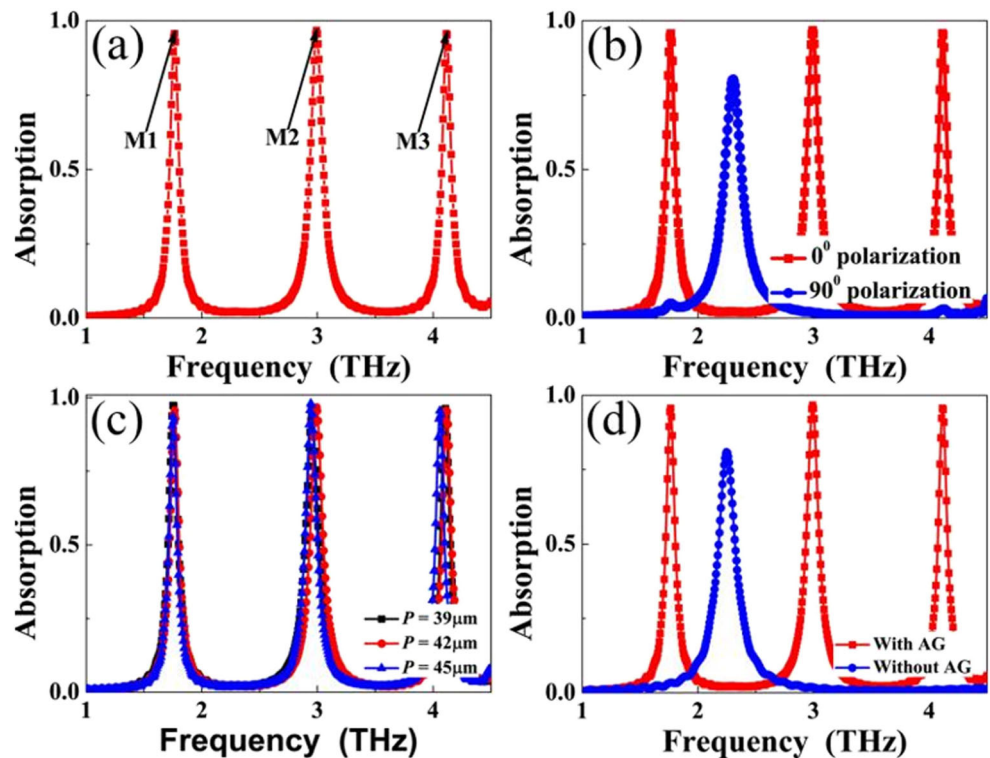

stacking several ASRRs. Figure 2 b gives the absorption spectra of the designed device in two orthogonal polarizations. As shown, only one absorption peak is obtained when the electric field of the incident light is parallel to the *y*-axis (i.e., 90° polarization), which is different from the case of 0° polarization (electric field polarized in *x*-axis) having triple-band absorption. Results indicate that the designed device is sensitive to the polarization angles of incident light, which can be explained by the asymmetry of the ASRR.

The dependence of the absorption spectra on period *P* changes of the absorber is given to preliminarily investigate the resonance mechanism of the triple-band absorption. As shown in Fig. 2c, the absorption properties (including resonance frequency and absorptivity) of modes M1, M2, and M3 are all nearly unchanged when period *P* is tuned from 39 to 45 μm in intervals of 3 μm. It is well known that the operating frequency of the localized resonance response of the resonator is insensitive to the change of period *P*. Therefore, the three absorption modes should be respectively attributed to three different localized resonances of the ASRR. We further provide the absorption responses of the Au square patch with/without the small rectangular notch (or air gap) to investigate whether the presence of air gap plays an important role in obtaining the triple-band absorption. That is to say, we would like to know the difference in their absorption properties, of course, which can provide a new perspective on the mechanism interpretation of the triple-band absorption. It can be seen from blue curve of Fig. 2d that only one absorption

peak at frequency of 2.25 THz with absorption of 80.94% can be obtained when there is without air gap in the square patch (i.e., Au patch structure or patch antenna structure [55, 56]), while the introduction of the air gap in the Au square patch (or ASRR) can lead to three discrete resonance bands, which suggests that the presence of air gap in the metallic patch is critical in realizing the triple-band absorption. Particularly, we noticed that the resonance frequency of metallic patch structure has no any overlap (or adjacence) with three peaks of the ASRR. This point states that the resonance mechanism of the triple-band absorption is quite different from that of single-band absorption of the metallic patch structure.

Fig. 3 a–c respectively give the field distributions of |*E*| (in the center plane of the metallic resonator), real *Ez* (in the center plane of the metallic resonator), and |*Hy*| (in the plane of *y* = 0) of the single-band absorption of the metallic patch structure. Both of the |*E*| in Fig. 3a and real *Ez* in Fig. 3b are symmetrically distributed at both sides of the metallic patch structure along the *x*-axis (see the dotted line frames in this resonator). We also observed that its |*Hy*| field is mostly gathered in the dielectric sheet of the device. These field distributions suggest that the single-band absorption peak originates from the magnetic resonance of the metallic patch structure. Additionally, the |*E*| distribution of the single-band absorption of the ASRR in 90° polarization (see blue curve in Fig. 2b) is shown in Fig. 3d. Its |*E*| field is mainly focused on the top and bottom sides of the resonator along the *y*-axis (see the dotted

Fig. 3 (**a**) The |E|, (**b**) real Ez, and (**c**) |Hy| field distributions of the resonance absorption peak in metallic patch resonator without air gap. (**d**) The |E| distribution of the designed triple-band absorption device in 90° polarization
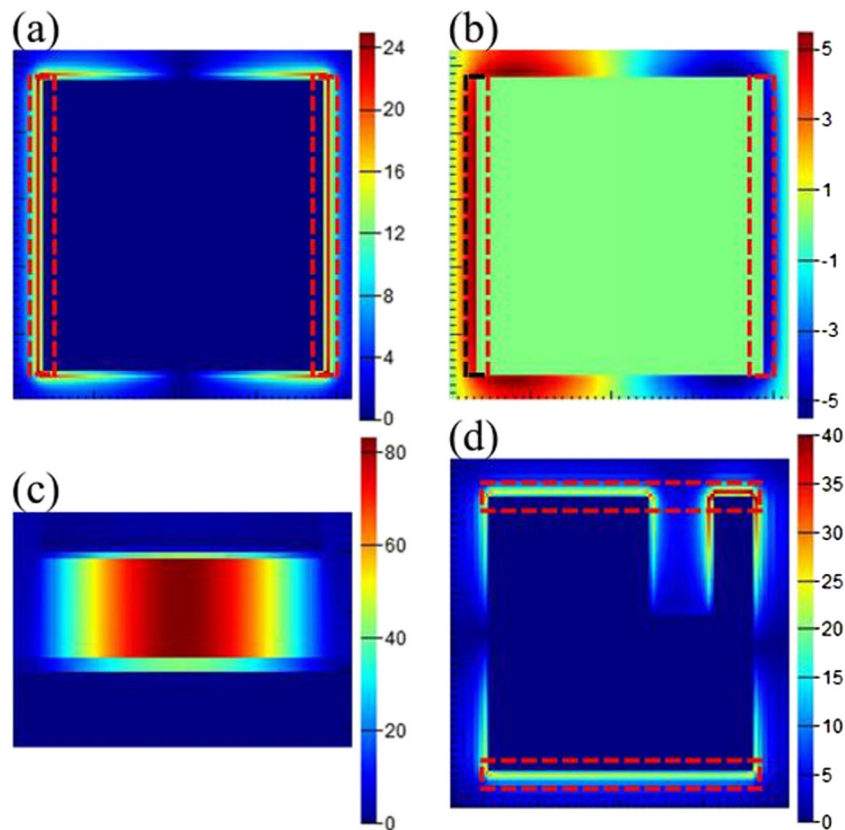
line frames in this resonator), which is very similar to that of the absorption of the metallic patch structure in 0° polarization along the x-axis. Therefore, the mechanism of the single-band absorption of the ASRR in 90° polarization should be due to the magnetic resonance of the metallic resonator.

To reveal the mechanism of the triple-band absorption, the corresponding field (|E| and real Ez) distributions of modes M1, M2, and M3 are provided in Fig. 4. As shown, the |E| and real Ez fields of the three modes are not symmetrically distributed at the sides of the ASRR, but are distributed over some

Fig. 4 The **a** |E| and **d** real Ez field distributions of mode M1 for the triple-band absorption device. The **b** |E| and **e** real Ez field distributions of mode M2 for the triple-band absorption device. The **c** |E| and **f** real Ez field distributions of mode M3 for the triple-band absorption device
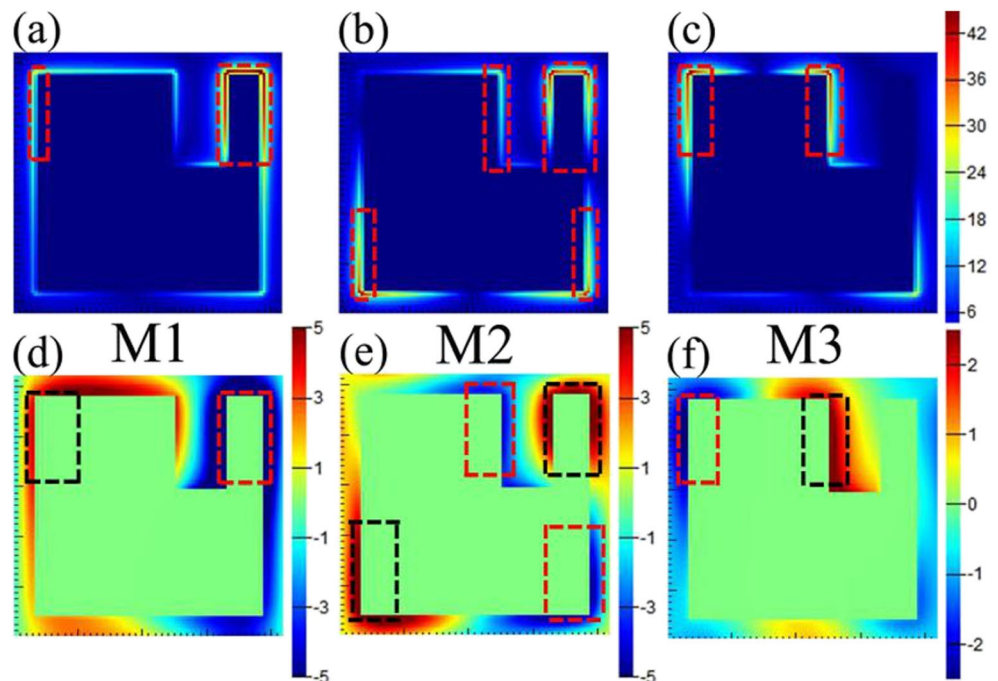
specific areas or sections of the resonator. Specifically, the $|E|$ field of mode M1 in Fig. 4a is mainly concentrated on both sides, in particular on the top both sides, of the ASRR (see the dotted line frames in this resonator), and its real Ez field in Fig. 4d has the similar distribution feature that is mostly focused on the top both sides of the resonator (see the dotted line frames in this resonator), which indicates that mode M1 is the electric dipole resonance of the ASRR. For resonance mode M2, we observed that the $|E|$ field of Fig. 4b (or real Ez field of Fig. 4e) is not only clustered in the bottom both sides of the ASRR but also both sides of the air gap of the metallic patch (see the dotted line frames in this resonator), which show that mode M2 should be attributed to the coupling of two different localized responses of the metallic resonator (or the electric quadrupole resonance of the ASRR). Different from the cases of modes M1 and M2, the $|E|$ field and real Ez field of mode M3 are both chiefly accumulated at the left-top both sides of the ASRR (see the dotted line frames in Fig. 4c, f), and thus mode M3 should be attributed to the electric resonance along the width of the wider arm of the ASRR coming from the non-symmetric notch position. Because the field distributions of the three modes are all gathered on both sides (or edges) of the different sections of the ASRR, modes M1, M2, and M3 should be attributed to the localized responses of different sections of the ASRR.

We also noticed that the $|E|$ and real Ez distributions of modes M1, M2, and M3 are totally different from the case of the single-band absorption of the metallic patch structure

in Fig. 3a, b that are equally distributed at both sides of the metallic patch structure, which show that the introduction of air gap in the metallic patch can destroy the original field distribution of the resonator, and therefore three new field distributions (or resonance modes) are introduced. That is to say, the presence of air gap in the metallic patch is a key factor in achieving the triple-band absorption. Certainly, the size changes of the air gap inevitably affect the performance of the device. As shown in Fig. 5a–c, the parameter changes of the air gap indeed affect the absorption properties of the triple-band device. However, different parameter variations of the air gap show different performance changes. The change of the air gap length g in Fig. 5a mainly influences mode M3, while the parameter change of the air gap width d in Fig. 5b (or air gap deviation value of △ in Fig. 5c) affects not only mode M3 but also modes M1 and M2. These change features show that the performance of the triple-band absorption can be controlled by employing different parameters of the air gap.

We further found that the metallic resonator length l also shows large influence on the absorption performance of the triple-band device. It can be seen from Fig. 5d that the resonance frequencies of the three modes are all blue-shift with the increase of length l, while the absorption strength changes of the three modes are negligible, which are different from the parameter variations of the air gap in Fig. 5a–c having large absorption strength changes. This kind of excellent absorption characteristic only regulates the resonance frequency without affecting the absorption strength and can be used to extend the

Fig. 5. Simulation results of the triple-band absorption device with the changes of the **a** g, **b** d, **c** △, and **d** l
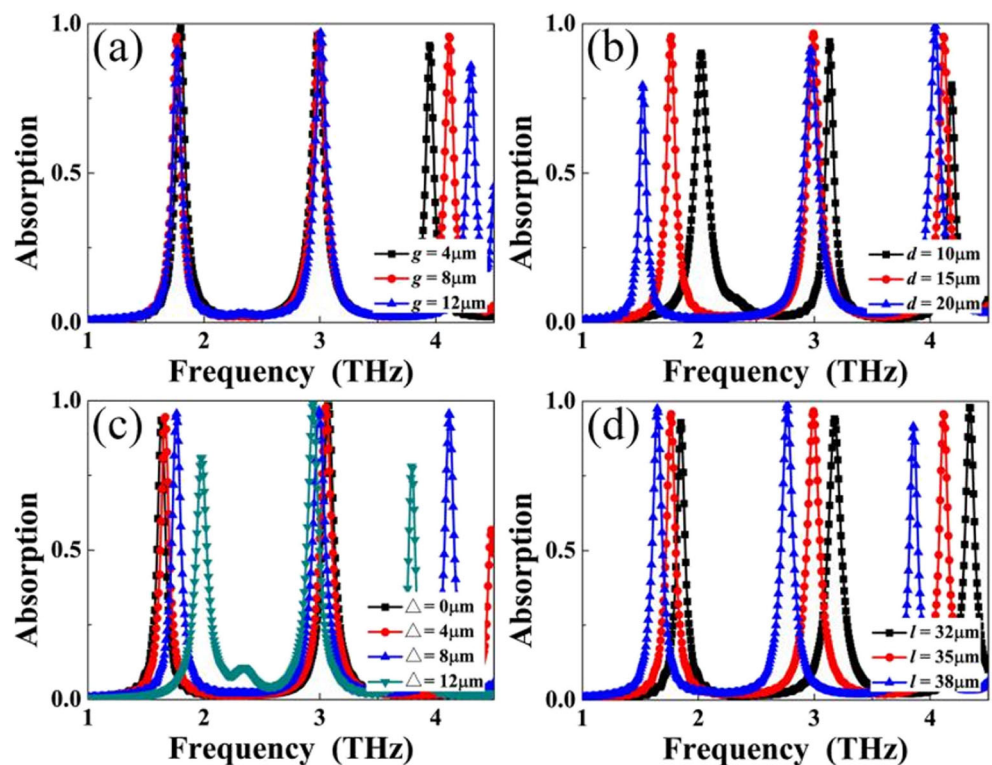
number of resonance peaks. As a special example, a six-band absorption device can be obtained by simply stacking two different dimensions of ASRRs. The detailed discussion of the six-band absorption device is presented in the next section of this manuscript.

As mentioned in the last two paragraphs of the "Design principles of the multiple-band perfect metamaterial absorber" section, it is quite difficult to realize more number of absorption peaks (larger than three) with large absorbance via introducing two or more air gaps in the metallic patch structure. To give the intuitive results, the resonance absorption curves under different number of air gaps (or different position of the air gaps) are given in Fig. 6. It should be noted that these air gaps have the same structure sizes, such as length g and width d. For Fig. 6a, it is found that the metallic patch with a single air gap (i.e., the designed ASRR) has the results of three discrete resonance peaks with large absorption rates, while metallic patch with two or more air gaps under different positions possess the ability to decrease the number of absorption peaks or reduce the absorption intensity of the resonance bands (see Fig. 6b–f). These results reveal that we cannot increase the number of absorption peaks through introducing more amounts of air gaps having different positions in the metallic patch. The cause of this phenomenon is given in the last paragraph of the "Design principles of the multiple-band perfect metamaterial absorber" section. As a result, the number of absorption peaks can be effectively increased by using stacked design strategy, as illustrated in the next two sections.

Design of Six-Band Terahertz Perfect Metamaterial Absorber

As discussed in Fig. 5d, the length l change of the ASRR can obviously affect the frequencies of the triple-band absorption device, while the strength changes of the three modes are negligible. Based on this, we can design a type of six-band terahertz absorption device by simply stacking two similar but different sizes of the ASRRs, where each layer of the ASRR possesses three discrete resonance peaks, and the combination of the two layers has the ability to achieve the six-band absorption. Figure 7 a gives the side view of the design of the dual-layer six-band absorption device. As shown, the basic cell of the device is consisted of two alternating stack of ASRRs and dielectric sheets on top of a metallic film. The top views of the first and second layer of the ASRR are given in Fig. 7b, c, respectively. The ASRRs in the first and second layer have lengths of $l_1 = 32$ μm and $l_2 = 40$ μm, respectively. The air gap in both layers of the metallic patch has the same parameters of $g = 8$ μm, $d = 15$ μm, and $\triangle = 8$ μm. The repeat period of the basic cell of the six-band device is $P = Px = Py = 45$ μm. The thicknesses of the first and the second,layer of the dielectric sheets are respectively $t_1 = 1.5$ μm and $t_2 = 2.2$ μm. The computational model, boundary conditions, and the material properties (including the metallic conductivity and the refractive index of the dielectric sheet) of the six-band terahertz absorption device are the same as the triple-band absorption in Fig. 1.
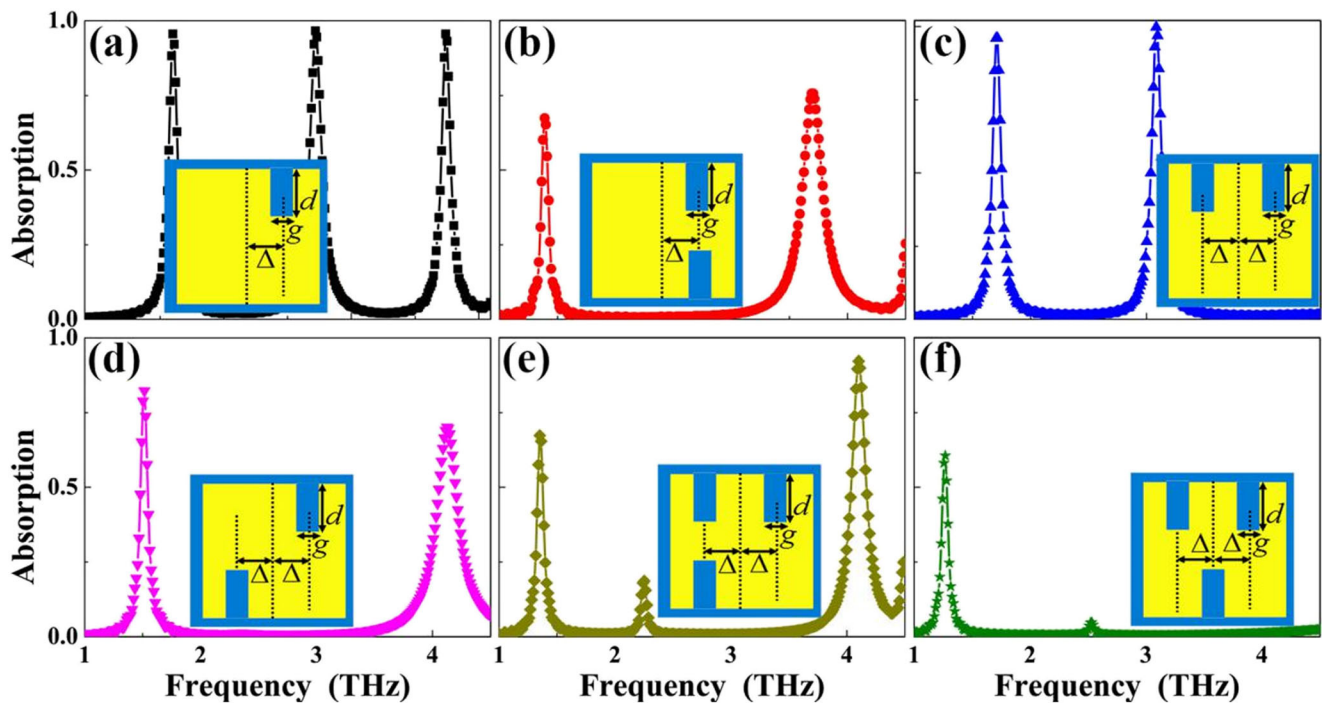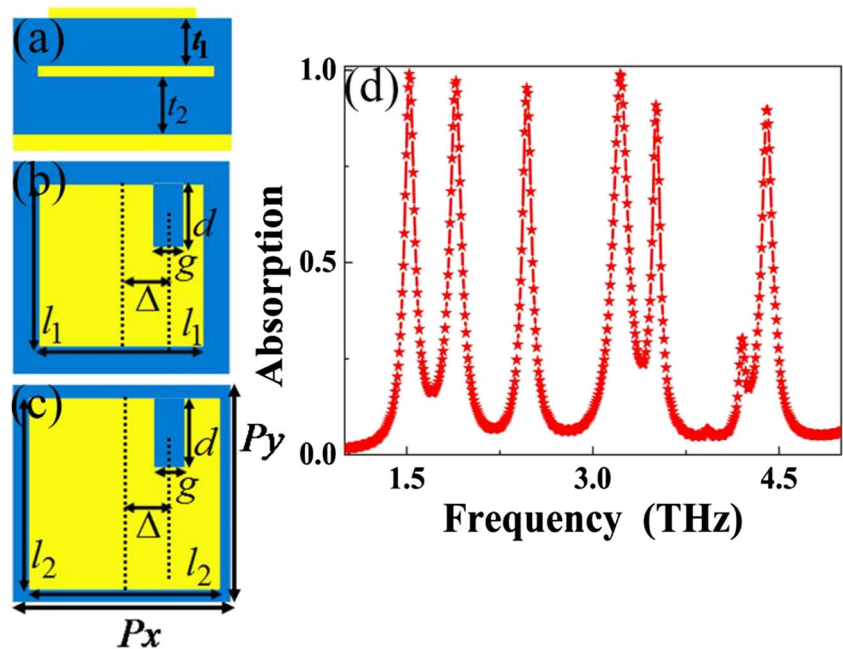

Fig. 6 (**a**), (**b**), (**c**), (**d**), (**e**), and (**f**) provide the resonance absorption curves under different number of air gaps (or different position of the air gaps). Insets of each figure are the top view of the basic cell of resonator with different number of air gaps (or different position of the air gaps)

Six discrete absorption peaks at resonance frequencies of
1.52 THz (M1), 1.90 THz (M2), 2.47 THz (M3), 3.22 THz
(M4), 3.51 THz (M5), and 4.41 THz (M6) with average ab-
sorption rates of 95.05% can be obtained in the simulation
result of Fig. 7d. The resonance bandwidths of the six discrete
modes are quite narrow, which are respectively 0.10 THz,
0.12 THz, 0.10 THz, 0.15 THz, 0.06 THz, and 0.11 THz,
and the corresponding Q values are 15.20, 15.83, 24.70,
21.47, 58.50, and 40.09, respectively. Compared with the res-
onance wavelengths of the six modes, furthermore, the dielec-
tric sheet thickness ($t_1 + t_2 = 3.7$ μm) of the six-band absorp-
tion device is very thin. The minimum (or maximum) reso-
nance wavelength of the six-band absorption device in mode
M6 (or M1) is about 18.39 (or 53.34) times of the dielectric

sheet, which reveals that the designed device has the reso-
nance feature of ultra-thin dielectric sheet thickness. Three
excellent properties of large absorption rates, narrow reso-
nance bandwidths, and the ultra-thin dielectric sheet thickness
of the six-band absorption device are very useful in practical
applications.

To explore and analyze the resonance mechanism of the
six-band terahertz absorption device, the corresponding $|E|$
field distributions of the six discrete modes are provided, as
shown in Fig. 8. The first row (or line) of Fig. 8 (defined as
L1) gives the $|E|$ distributions of the six modes in the center
plane of the first layer of ASRR, while the $|E|$ distributions in
the center plane of the second layer of ASRR are shown in the
second row (or line) of Fig. 8 (defined as L2). It can be seen
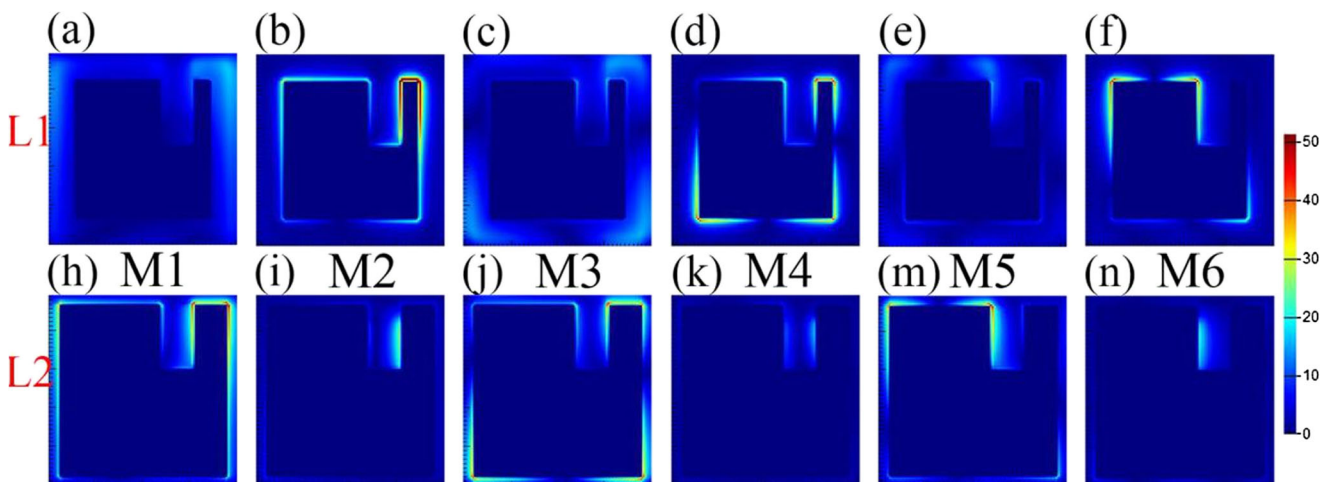
Fig. 8 The $|E|$ field distributions of modes M1(a), M2 (b), M3 (c), M4 (d), M5 (e), and M6 (f) of the first layer of ASRR. The $|E|$ field distributions of
modes M1 (h), M2 (i), M3 (j), M4 (k), M5 (m), and M6 (n) of the second layer of ASRR

from L1 and L2 that the $|E|$ field distributions of the six discrete modes are mostly focused on the edges of the ASRRs in the dual-layer resonance structure, which prove that these modes are caused by the localized resonance responses of the two ASRRs. However, the $|E|$ field distributions of each resonance mode of the six-band device in the dual-layer ASRRs are different. To be specific, for the first resonance mode M1, its $|E|$ field is mainly gathered in the edges of the ASRR in the second layer, while the $|E|$ field in first layer of the ASRR can be neglected (see Fig. 8a, h). For mode M2, we observed that its $|E|$ field is primarily concentrated on the first layer of the ASRR (see Fig. 8b), whereas the second layer of the ASRR has a neglected field distribution (see Fig. 8i). The $|E|$ fields of modes M3 and M4 are mainly respectively focused on the second layer of the ASRR in Fig. 8j and the first layer of the ASRR in Fig. 8d.

Different from the cases of modes M3 and M4, the field distributions of modes M5 and M6 are primarily clustered in the edges of the ASRR in the second layer and the first layer, respectively (see Fig. 8m, f). According to these electric field distribution characteristics, we can conclude that modes M1, M3, and M5 are mainly associated with excitation of the second layer of the ASRR (i.e., the L2), while modes M2, M4, and M6 are primarily the consequence of excitation of the ASRR in the first layer (i.e., the L1). We particularly found that the field distributions of modes M1, M3, and M5 (or modes M2, M4, and M6) in the second layer of the ASRR (or first layer of the ASRR) are respectively similar to that of modes M1, M2, and M3 of the triple-band terahertz absorption device in Fig. 4, which indicates that each layer of the dual-layer structure corresponds to three different resonance modes, the combination effect of the two sets of the three resonance modes leads to the six-band absorption response.

Because modes M1, M3, and M5 (or modes M2, M4, and M6) are determined by the ASRR in the second layer (or the first layer), the dimension changes of the ASRR inevitably affect the resonance frequencies of the six-band device. For example, the length change of the first layer of the ASRR should provide the ability to tune the resonance frequencies of M2, M4, and M6 of the six-band absorption device, while the resonance frequencies of modes M1, M3, and M5 should be controlled by the size of the ASRR in the second layer. Simulation results of Fig. 9a show that the resonance frequencies of modes M2, M4, and M6 indeed can be affected through the length l_1 change of the ASRR in the first layer, while the frequency shifts of modes M1, M3, and M5 are nearly neglected. We further found that length l_2 variation of the ASRR in the second layer can evidently influence the absorption performance of modes M2, M4, and M6, whereas the absorption response changes of other modes (M1, M3, and M5) are negligible (see Fig. 9b). Dependence of the absorption performance on the length changes of the ASRR can provide new path to control the resonance frequencies of the six-band absorption device and can broaden the application abilities of the device.

Design of More Number of Absorption Peaks

This section indicates that the six-band light absorber can be obtained by stacking two layers of ASRRs. It is predicted that more amounts of absorption peaks can be realized by stacking one more ASRR (i.e., three layers of ASRRs). To verify this prediction, this section gives the design of three layers of ASRRs, and its side view is demonstrated in Fig. 10a. As revealed, the basic cell of the three-layer structure has three alternating stack of ASRRs and dielectric gaps atop of a metallic board. The top views of the first, second, and third layer of the ASRR are respectively shown in Fig. 10b–c. The lengths of these ASRRs in the first, second, and third layer are respectively $l_1 = 28\ \mu m$, $l_2 = 38\ \mu m$, and $l_3 = 58\ \mu m$. The thicknesses
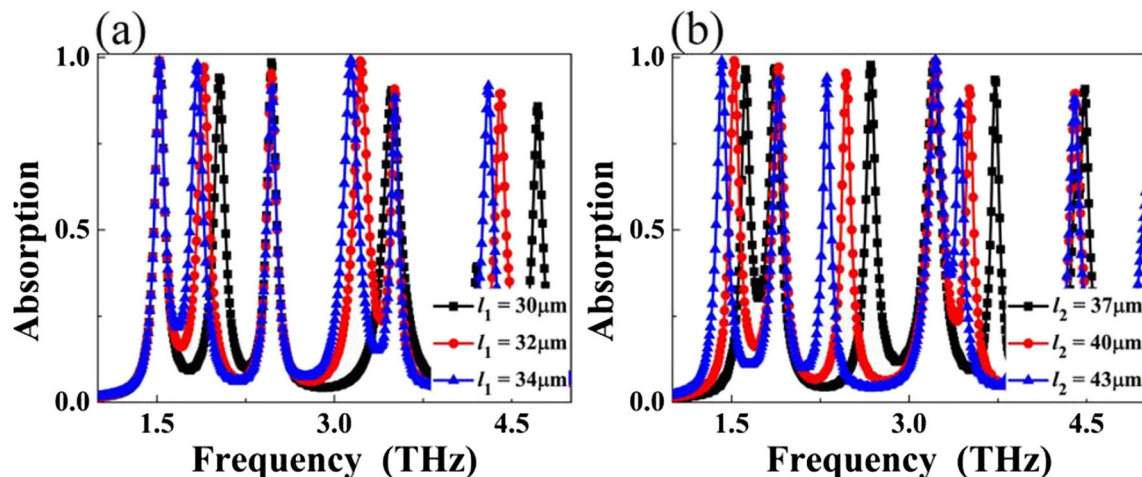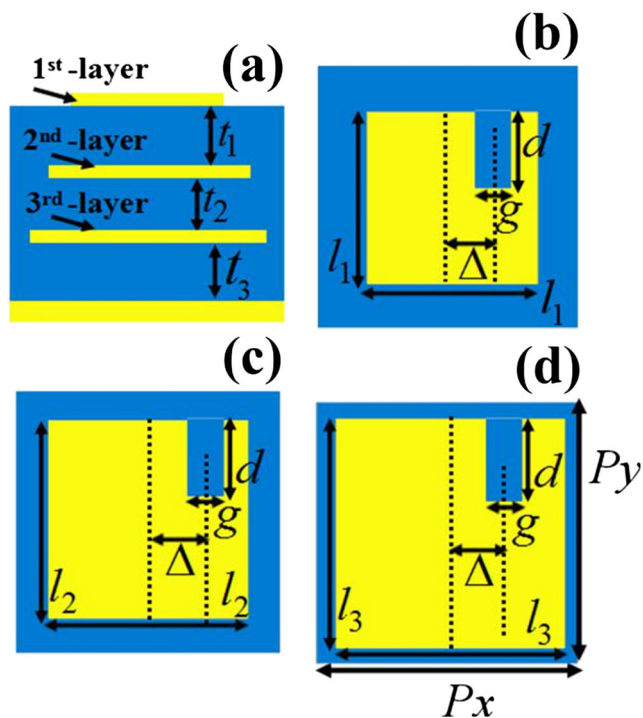

Fig. 9 The simulation results of the designed six-band absorption device with the changes of l_1 (a) and l_2 (b)

Fig. 10 (a) Side view of the basic cell of the three-layer structure. Top views of the first (b), second (c), and third (d) layer of the ASRR

of the three dielectric gaps in the first, second, and third layer are $t_1 = 2.1$ μm, $t_2 = 3$ μm, and $t_3 = 2.2$ μm. The air gap in the three layers of the ASRRs has the same sizes of $g = 8$ μm, $d = 15$ μm, and $\triangle = 8$ μm. The basic cell of the three-layer structure has the period of $P = Px = Py =$

66 μm. Other structure parameters, including dielectric constant of the dielectric gap and conductivity of the metallic layer, are the same as the triple-band absorption device in Fig. 1.

The absorption response of the three layers of the ASRRs is shown in Fig. 11a; it is observed that eight absorption peaks centered at M1 = 1.16 THz, M2 = 1.56 THz, M3 = 1.76 THz, M4 = 2.01 THz, M5 = 2.55 THz, M6 = 3.43 THz, M7 = 3.74 THz, and M8 = 3.99 THz having the absorption coefficients of 98.07%, 98.06%, 67.51%, 95.75%, 98.66%, 95.68%, 95.55%, and 95.49% are gained, respectively; the average absorption coefficients of the eight absorption modes are greater than 93.10%. Compared with the two layers of ASRRs having six-band absorption, it is clear that more absorption peaks can be obtained by employing three layers of ASRRs.

Simulation results further prove that the length change of each layer of ASRR can provide large influence on the resonance performance of the eight-band absorption device. For example, the length (l_1) variation of the first layer of ASRR in Fig. 11b mainly affects the resonance performance of modes M4, M6, and M7, while the changes of the other modes are negligible. This indicates that the forming mechanisms of modes M4, M6, and M7 should be derived from the resonance responses of the first layer of ASRR. The physical causes of modes M2, M5, and M8 should be due to the second layer of ASRR because its length l_2 plays a vital role in controlling the resonance frequencies of modes M2, M5, and M8 of the eight-band

Fig. 11 (a) Absorption response of the three layers of the ASRRs. Absorption response of the three layers of the ASRRs under different length variations of l_1 (b), l_2 (c), and l_3 (d)
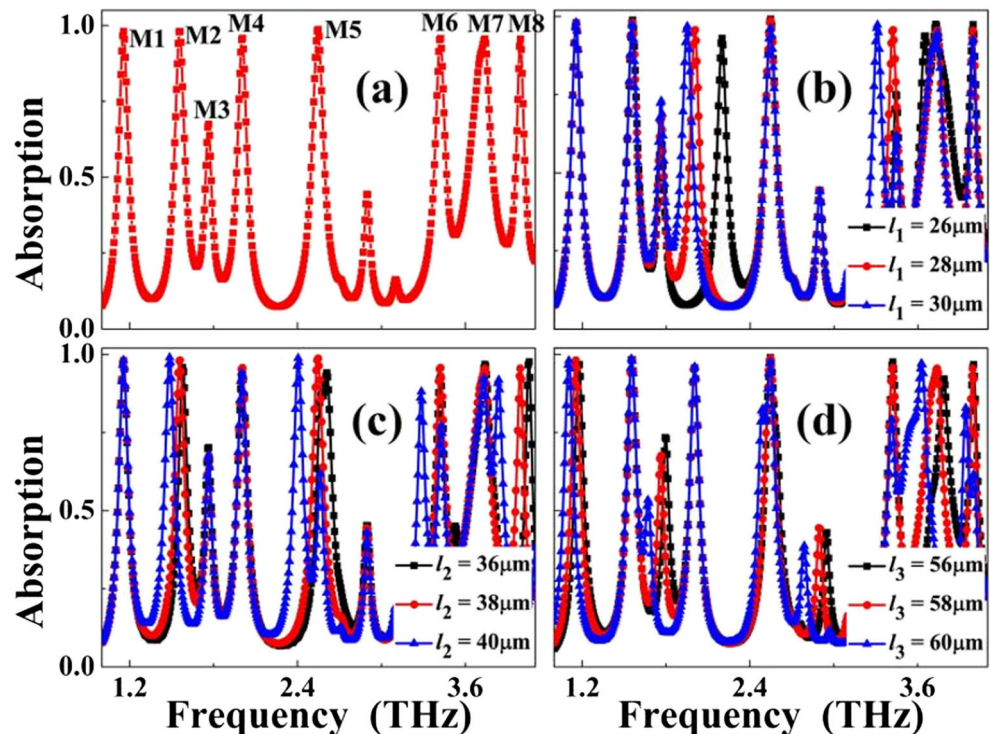
absorption device (see Fig. 11c). Similarly, the resonance peaks at modes M1, M3, and M7 should be primarily associated with the excitation of the third layer of ASRR because the change in length l_3 can remarkably affect the three absorption bands (see Fig. 11d).

Conclusions

This paper presents the study of the triple-band perfect absorption device in the terahertz region. The unit cell of the device can be designed through utilizing an Au square patch with a small rectangular notch (or ASRR), 1.7-μm thickness of insulating dielectric sheet, and a continuous metallic film. The presented device can offer three discrete absorption peaks with large absorption, narrow resonance bandwidth, ultra-thin dielectric layer thickness, and simple structure design. The corresponding field distributions of the three resonance modes are given as insight into the resonance mechanism of the triple-band absorption device. We also noted that the parameter changes of the ASRR (in particular of its length) can obviously affect the absorption performance of the triple-band absorption device. Based on this feature, a kind of six-band terahertz absorption device is presented through stacking two similar but different dimensions of ASRRs. Each metallic layer of the ASRR corresponds to three separated absorption modes, and the superposition of two sets of three resonance bands in the dual-layer structure leads to the six-band absorption. Further results prove that the length variations of the two ASRRs in the dual-layer structure can provide the ability to tune or control the frequencies of the six-band absorption device. The multiple-band terahertz metamaterial absorbers demonstrated here can find application prospects in many fields, such as opto-electronic and engineering.

Compliance with Ethical Standards

Conflict of Interest The authors declare that they have no conflict of interest.

References

1. Yong Z, Zhang S, Gong C, He S (2016) Narrow band perfect absorber for maximum localized magnetic and electric field enhancement and sensing applications. Sci Rep 6:24063

2. Chen WC, Cardin A, Koirala M, Liu X, Tyler T, West KG, Bingham CM, Starr T, Starr AF, Jokerst NM, Padilla WJ (2016) Role of surface electromagnetic waves in metamaterial absorbers. Opt Express 24:6783

3. Chen HT (2012) Interference theory of metamaterial perfect absorbers. Opt Express 20:7165–7172

4. Huang L, Chowdhury DR, Ramani S, Reiten MT, Luo SN, Azad AK, Taylor AJ, Chen HT (2012) Impact of resonator geometry and its coupling with ground plane on ultrathin metamaterial perfect absorbers. Appl Phys Lett 101:101102

5. Faniayeu I, Mizeikis V (2017) Vertical split-ring resonator perfect absorber metamaterial for IR frequencies realized via femtosecond direct laser writing. Appl Phys Express 10:062001

6. Wu PC, Liao CY, Chen JW, Tsai DP (2017) Isotropic absorption and sensor of vertical split-ring resonator. Adv Opt Mater 5: 1600581

7. Wang BX (2017) Quad-band terahertz metamaterial absorber based on the combining of the dipole and quadrupole resonances of two SRRs. IEEE J Select Quantum Electron 23:4700107

8. Liu X, Bi K, Li B, Zhao Q, Zhou J (2016) Metamaterial perfect absorber based on artificial dielectric atoms. Opt Express 24: 20454–20460

9. Chang YC, Kildishev AV, Narimanov EE, Norris TB (2016) Metasurface perfect absorber based on guided resonance of a photonic hypercrystal. Phys Rev B 94:155430

10. Fan K, Suen JY, Liu X, Padilla WJ (2017) All-dielectric metasurface absorbers for uncooled terahertz imaging. Optic 4:601

11. Liu X, Fan K, Shadrivov IV, Padilla WJ (2017) Experimental realization of a terahertz all-dielectric metasurface absorber. Opt Express 25:191–201

12. Zhao X, Zhang J, Fan K, Duan G, Metcalfe GD, Wraback M, Zhang X, Averitt RD (2016) Nonlinear terahertz metamaterial perfect absorbers using GaAs. Photon Res 4:A16

13. Watts CM, Liu X, Padilla WJ (2012) Metamaterial electromagnetic wave absorbers. Adv Mater 24:OP98

14. Wang BX, Zhai X, Wang GZ, Huang WQ, Wang LL (2015) Frequency tunable metamaterial absorber at deep-subwavelength scale. Opt Mater Express 5:227

15. Hu X, Xu G, Wen L, Wang H, Zhao Y, Zhang Y, Cummong DRS, Chen Q (2016) Metamaterial absorber integrated microfluidic terahertz sensors. Laser Photon Rev 10:962–969

16. Kajtar G, Kafesaki M, Economou EN, Soukoulis CM (2016) Theoretical model of homogeneous metal-insulator-metal perfect multi-band absorbers for the visible spectrum. J Phys D 49:055104

17. Liu S, Zhuge J, Ma S, Chen H, Bao D, He Q, Zhou L, Cui TJ (2016) A bi-layered quad-band metamaterial absorber at terahertz frequencies. J Appl Phys 118:245304

18. Li X, Lan C, Bi K, Li B, Zhao Q, Zhou J (2016) Dual band metamaterial perfect absorber based on Mie resonances. Appl Phys Lett 109:062902

19. Yao G, Ling F, Yue J, Luo C, Ji J, Yao J (2016) Dual-band tunable perfect metamaterial absorber in the THz range. Opt Express 24: 1518–1527

20. Wang BX, Zhai X, Wang GZ, Huang WQ, Wang LL (2015) A novel dual-band terahertz metamaterial absorber for a sensor application. J Appl Phys 117:014504

21. Astorino MD, Frezza F, Tedeschi N (2017) Ultra-thin narrow-band, complementary narrow-band, and dual-band metamaterial absorbers for applications in the THz regime. J Appl Phys 121:063103

22. Wang BX, Wang GZ, Wang LL (2016) Design of a novel dual-band terahertz metamaterial absorber. Plasmonics 11:523–530

23. Liu X, Lan C, Li B, Zhao Q, Zhou J (2016) Dual band metamaterial perfect absorber based on artificial dielectric molecules. Sci Rep 6: 28906

24. Wang BX, Wang GZ, Sang T (2016) Simple design of novel triple-band terahertz metamaterial absorber for sensing application. J Phys D 49:165307

25. Zhang N, Zhou P, Cheng D, Weng X, Xie J, Deng L (2013) Dual-band absorption of mid-infrared metamaterial absorber based on distinct dielectric spacing layers. Opt Lett 38:1125–1127

26. Shen X, Cui TJ, Zhao J, Ma HF, Jiang WX, Li H (2011) Polarization-independent wide-angle triple-band metamaterial absorber. Opt Express 19:9401

27. Shen X, Yang Y, Zang Y, Gu J, Han J, Zhang W, Cui TJ (2012) Triple-and terahertz metamaterial absorber: design, experiment, and physical interpretation. Appl Phys Lett 101:154102

28. Xu J, Zhao Z, Yu H, Yang L, Gou P, Cao J, Zou Y, Qian J, Shi T, Ren Q, An Z (2016) Design of triple-band metamaterial absorbers with refractive index sensitivity at infrared frequencies. Opt Express 24:25742–25751

29. Wang GD, Chen JF, Hu XW, Chen ZQ, Liu MH (2014) Polarization-insensitive triple-band microwave metamaterial absorber based on rotated square rings. Prog Electromagn Res 145: 175–183

30. Wang BX, Zhai X, Wang GZ, Huang WQ, Wang LL (2015) Design of a four-band and polarization-insensitive terahertz metamaterial absorber. IEEE Photon J 7:4600108

31. Bhattacharyya S, Srivastava KV (2014) Triple band polarization-independent ultra-thin metamaterial absorber using electric field-driven LC resonator. J Appl Phys 115:064508

32. Huang X, Yang H, Yu S, Wang J, Li M, Ye Q (2013) Triple-band polarization-insensitive wide-angle ultra-thin planar spiral metamaterial absorber. J Appl Phys 113:213516

33. Bhattacharyya S, Ghosh S, Srivastava KV (2013) Triple band polarization-independent metamaterial absorber with bandwidth enhancement at X-band. J Appl Phys 114:094514

34. Park JW, Tuong PV, Rhee JY, Kim KW, Jang WH, Choi EH, Chen LY, Lee YP (2013) Multi-band metamaterial absorber based on the arrangement of donut-type resonators. Opt Express 21:9691

35. Chen J, Hu Z, Wang S, Huang X, Liu M (2016) A triple-band, polarization- and incident angle-independent microwave metamaterial absorber with interference theory. Eur Phys J B 89:14

36. Zhang B, Hendrickson J, Guo J (2013) Multispectral near-perfect metamaterial absorbers using spatially multiplexed plasmon resonance metal square structures. J Opt Soc Am B 30:656

37. Kollatou TM, Dimitriadis AI, Assimonis SD, Kantartzis NV, Antonopoulos CS (2014) Multi-band, high absorbing, microwave metamaterial structures. Appl Phys A Mater Sci Process 115:555–561

38. Ma B, Liu S, Bian B, Kong X, Zhang H, Mao Z, Wang B (2014) Novel three-band microwave metamaterial absorber. J Electromagn Waves Appl 28:1478–1486

39. Zhai H, Zhan C, Li Z, Liang C (2015) A triple-band ultrathin metamaterial absorber with wide-angle and polarization stability. IEEE Antennas Wireless Propag Lett 14:241–244

40. Arezoomand AS, Zarrabi FB, Heydari S, Gandji NP (2015) Independent polarization and multi-band THz absorber base on Jerusalem cross. Opt Commun 352:121–126

41. Mishra N, Choudhary DK, Chowdhury R, Kumari K, Chaudhary RK (2017) An investigation on compact ultra-thin triple-band polarization independent metamaterial absorber for microwave frequency applications. IEEE Access 5:4370–4376

42. Sarkhel, A.; Chaudhuri, S.R.B. 2015 Design of a compact triple-band metamaterial absorber with wide angle of incidence using connected resonator topology. 2015 International Conference on Electromagnetics in Advanced Applications, 1239 https://ieeexplore.ieee.org/abstract/document/7297316. Accessed 13 June 2019

43. Ghosh, S.; Bhattacharyya, S.; Kaiprath, Y.; Chuaurasiya, D.; Srivastava, K.V. 2015 Triple-band polarization-independent metamaterial absorber using destructive interference. Proceedings of the 45th European Microwave Conference, 7–10 Sep., Paris, France, 335 https://ieeexplore.ieee.org/abstract/document/7345768. Accessed 13 June 2019

44. Shang S, Yang S, Tao L, Yang L, Cao H (2016) Ultrathin triple-band polarization-insensitive wide-angle compact metamaterial absorber. AIP Adv 6:075203

45. Sharma SK, Ghosh S, Srivastava KV (2016) An ultra-thin triple-band polarization-insensitive metamaterial absorber for S, C, and X band applications. Appl Phys A Mater Sci Process 122:1071

46. Bowen PT, Baron A, Simth DR (2016) Theory of patch-antenna metamaterial perfect absorbers. Phys Rev A 93:063849

47. Cheng Y, Nie Y, Gong R (2013) A polarization-insensitive and omnidirectional broadband terahertz metamaterial absorber based on coplanar multi-squares films. Opt Laser Technol 48:415–421

48. Hendrickson J, Guo J, Zhang B, Buchwald W, Soref R (2012) Wideband perfect light absorber at midwave infrared using multiplexed metal structures. Opt Lett 37:371–373

49. Viet DT, Hien NT, Tuong PV, Minh NQ, Trang PT, Le LN, Lee YP, Lam VD (2014) Perfect absorber metamaterials: peak, multi-peak and broadband absorption. Opt Commun 322:209–213

50. Liu Y, Gu S, Luo C, Zhao X (2012) Ultra-thin broadband metamaterial absorber. Appl Phys A Mater Sci Process 108:19–24

51. Linden S, Enkrich C, Wegener M, Zhou J, Koschn T, Soukoulis CM (2004) Magnetic response of metamaterials at 100 terahertz. Science 306:1351–1353

52. Sersic I, Frimmer M, Verhagen E, Koenderink AF (2009) Electric and magnetic dipole coupling in near-infrared split-ring metamaterial arrays. Phys Rev Lett 103:213902

53. Padilla WJ, Taylor AJ, Highstrete C, Lee M, Averitt RD (2006) Dynamical electric and magnetic metamaterial response at terahertz frequencies. Phys Rev Lett 96:107401

54. Wang BX, Wang GZ, Wang LL, Zhai X (2016) Design of a five-band terahertz absorber based on three nested split-ring resonators. IEEE Photon Technol Lett 28:307–310

55. Huang YW, Chen WT, Tsai WY, Wu PC, Wang CM, Sun G, Tsai DP (2015) Aluminum plasmonic multicolor meta-hologram. Nano Lett 15:3122–3127

56. Huang YW, Lee HWH, Sokhoyan R, Pala RA, Thyagarajan K, Han S, Tsai DP, Atwater HA (2016) Gate-tunable conducting oxide metasurfaces. Nano Lett 16:5319–5325